SCIENCE CHINA Materials ARTICLES

mater.scichina.com link.springer.com

Published online 27 May 2021 | https://doi.org/10.1007/s40843-021-1647-0
Sci China Mater 2021, 64(10): 2551–2562

$(Bi,Sb)_2Te_3$/SiC nanocomposites with enhanced thermoelectric performance: Effect of SiC nanoparticle size and compositional modulation

Bowen Cai[1], Jun Pei[1], Jinfeng Dong[1], Hua-Lu Zhuang[1], Jinyu Gu[1], Qian Cao[2], Haihua Hu[1], Zihao Lin[1] and Jing-Feng Li[1*]

ABSTRACT Fabrication of nanoparticle-dispersed composites is an effective strategy for enhancing the performance of thermoelectric materials, and in particular SiC nanoparticles have been often used to create composites with Bi_2Te_3-based applied thermoelectric materials. However, the effect of particle size on the thermoelectric performance is unclear. This work systematically investigated the electrical and thermal properties of a series of $(Bi,Sb)_2Te_3$-based nanocomposites containing dispersed SiC nanoparticles of different sizes. It was found that particle size has a significant impact on the electrical properties with smaller SiC nanoparticles giving rise to higher electrical conductivity. Even though the dispersed SiC nanoparticles enhanced the Seebeck coefficient, no apparent dependence of the enhancement on the particle size was observed. It was also found that smaller SiC nanoparticles scatter phonons to some extent while the larger nanoparticles contribute to increased thermal conductivity. Eventually, the highest *ZT* value of 1.12 was obtained in 30 nm-SiC dispersed sample, corresponding to an increase by 18% from 0.95 for the matrix made from commercial scraps, and then the *ZT* was further boosted to 1.33 by optimizing the matrix composition and expelling excess Te during the optimized spark plasma sintering process. This work proves that the dispersion of smaller SiC nanoparticles in p-type $(Bi,Sb)_2Te_3$ materials is more effective than the dispersion of larger nanoparticles. In addition, it is revealed that additional compositional and/or processing optimization is vital and effective for obtaining further performance enhancement for nanocomposites of SiC nanoparticles dispersed in $(Bi,Sb)_2Te_3$.

Keywords: thermoelectric materials, bismuth telluride, effect of SiC nanoparticle size, compositional and processing optimization

INTRODUCTION

Thermoelectric (TE) materials function as a bridge between heat and electricity, and show great potential for applications such as deep space exploration, wearable electronic devices and microsensors [1–4]. Therefore, TE material research has attracted increasing attention from both industry and academia. The TE performance of a material is often evaluated using the dimensionless figure of merit $ZT = S^2\sigma T/\kappa_{tot}$, where S, T, σ, and κ_{tot} are the Seebeck coefficient, absolute temperature, electrical conductivity, and total thermal conductivity, respectively. The total thermal conductivity mainly consists of the contributions of the charge carriers (κ_e) and lattice vibrations (κ_{lat}), and the bipolar thermal conductivity (κ_b) is also included in some cases [5–7]. Achieving high ZT values is challenging because of the strong coupling of S, σ, and κ_{tot} (mainly κ_e). Nevertheless, great progress has been made in improving the ZT values using a variety of methods such as nanostructure engineering [8–10], electronic band engineering [11–13], energy-filtering effect [14–17], defects engineering [18–21], as well as seeking or exploring materials with intrinsically low thermal conductivity [22–26].

Among various TE materials, Bi_2Te_3-based compounds have shown the best performance. These materials have been most widely used due to their outstanding advantages in electronic cooling and low-temperature waste heat harvesting and conversion, and have been commercialized successfully [27]. Many studies have shown that fabrication of nanocomposites through the dispersion of nanoparticles into the p-type $(Bi,Sb)_2Te_3$ matrix is an effective method for obtaining improved TE properties

---

[1] State Key Laboratory of New Ceramics and Fine Processing, School of Materials Science and Engineering, Tsinghua University, Beijing 100084, China

[2] Huabei Cooling Device Co. Ltd., Langfang 065400, China

[*] Corresponding author (email: jingfeng@mail.tsinghua.edu.cn)

[17,28–30]; however, the relationship between the nanoparticle size and TE properties is still unclear. Intuitively, nanoparticles with an appropriate size should have a stronger and more beneficial effect on the TE performance. On the other hand, because the TE properties are sensitive to material compositions [31,32], a fixed matrix composition is favorable for investigating the effect of the nanoparticle size on the TE properties. SiC has a wide band gap and low cost, and ultrafine SiC particles can be easily obtained. Moreover, SiC is thermally stable, thus avoiding the growth of SiC nanoparticles during high-temperature operation. Previous research on SiC nanoparticles dispersed in p-type $(Bi,Sb)_2Te_3$ has shown that 0.4 vol% is the optimal content for nano-SiC that produces a significant energy-filtering effect and contributes to the TE performance enhancement [17,33,34]. Recently, it has been claimed that expelling excess Te during spark plasma sintering (SPS) is beneficial for the enhancement of the TE performance of $(Bi,Sb)_2Te_3$ materials [35–37]. Thus, a combination of both strategies may provide an exceptional *ZT* enhancement effect.

In this work, we fixed the matrix composition by using commercial p-type $(Bi,Sb)_2Te_3$ scraps, and fabricated nano-SiC/$(Bi,Sb)_2Te_3$ composites *via* a simple method that combines ball milling (BM) and SPS, and investigated the effect of the particle size of the SiC nanoparticles on the TE performance. It is found that the dispersion of finer SiC nanoparticles results in a higher electrical conductivity compared with the dispersion of coarser SiC nanoparticles. The dispersion of SiC nanoparticles gives rise to an increased Seebeck coefficient that appears to be independent of the nanoparticle size. Additionally, the finer SiC nanoparticles result in a more prominent phonon-scattering effect than the coarser nanoparticles. All of the nano-SiC dispersed samples show higher *ZT* values than the sample without nano-SiC. The p-type $(Bi,Sb)_2Te_3$ with the finest dispersed SiC nanoparticles (30 nm) shows the highest *ZT* value of 1.12. Moreover, based on the sample with 30 nm-SiC dispersion, the matrix composition of the commercial p-type $(Bi,Sb)_2Te_3$ was modulated to expel the intentionally introduced excess Te. A higher *ZT* value of 1.33 was achieved under the optimized SPS conditions.

EXPERIMENTAL SECTION

As in our previous work, we used p-type $(Bi,Sb)_2Te_3$ scraps supplied by Huabei Cooling Device Co. Ltd. (China) in the experiments [34]. It should be noted that the raw scraps contain Se element even though it is usually used as n-type dopant. We performed the inductively coupled plasma-mass spectrometry (ICP-MS) experiment, which showed the chemical composition of the raw BiSbTe materials is $Bi_{0.48}Sb_{1.43}Te_3Se_{0.05}$. SiC nanoparticles with average sizes of 30, 100, and 700 nm were used. It is important to note that the SiC nanoparticles consist of different crystal types with 3C-SiC as the main crystal structure. The SiC nanoparticles with the sizes of 30 and 100 nm contain a slightly different 4H-SiC phase while the SiC nanoparticles with the size of 700 nm contain a small amount of the 6H-SiC phase (shown in Fig. S1). The p-type $(Bi,Sb)_2Te_3$ scraps were pulverized and mixed with SiC nanoparticles to obtain $(Bi,Sb)_2Te_3$ + 0.4 vol% SiC mixtures by BM for 3 h at 450 r min^{-1} in a stainless-steel jar. The ball-milled powders were sintered into cylindrical pellets with a diameter of 12 mm and a height of ~10 mm by SPS (SPS-211Lx, Fuji Electronic Industrial Co., Ltd., Japan) at 673 K under 50 MPa for 5 min in a vacuum.

X-ray diffraction (XRD, Cu Kα, Rigaku 2500, Japan) was used to analyze the crystal structure, and scanning electron microscopy (SEM, Zeiss Merlin, Germany) was used to characterize the morphologies of the samples. A transmission electron microscope (TEM, JEM-2100F, JEOL, Japan) equipped with an energy dispersive spectrometer (EDS) was used for microstructure observation and composition analysis. The σ and S were measured simultaneously using a ZEM-3 apparatus (Ulvac-Riko, Japan). The κ_{tot} was calculated according to $\kappa_{tot} = DC_Pd$ using the thermal diffusion coefficient (D) measured by the laser flash method (LFA 457, Netzsch, Germany). The measurement uncertainties for σ, S and D are approximately 5%, and the measurements were conducted along the direction perpendicular to the SPS compression because the TE performance along this direction is always superior to that along the parallel direction for polycrystalline $(Bi,Sb)_2Te_3$, as has been extensively confirmed in previous studies [37–39]. The mass density (d) was obtained by the Archimedes method. The specific heat at constant pressure (C_P) was calculated according to the Dulong-Petit law. The Wiedemann-Franz law $\kappa_e = L\sigma T$ was used to calculate the carrier thermal conductivity (κ_e), with the Lorenz factor (L) roughly estimated as $L = 1.5 + \exp(-|S|/116)$. Considering that the other uncertainties for C_P and d are small, the integrated uncertainty of the calculated *ZT* value is approximately 20%. The Hall carrier concentration (n_H) and mobility (μ_H) in the temperature range from room temperature to 475 K were obtained according to $n_H = 1/(eR_H)$ and $\mu_H = \sigma R_H$, respectively, with the Hall coefficient (R_H) determined using a Hall measurement system (ResiTest 8340DC, Toyo, Japan). A physical property measurement system (PPMS, Quantum Design Inc., USA) was used to measure the low-temperature electrical resistivity and thermal conductivity.

RESULTS AND DISCUSSION

TE performance of nanocomposites fabricated from commercially available $(Bi,Sb)_2Te_3$ with SiC nanoparticles of different sizes

Fig. 1a shows the XRD patterns of the commercially available p-type $(Bi,Sb)_2Te_3$ with dispersed SiC nanoparticles of different sizes. All of the diffraction peaks match well the standard PDF card of $Bi_{0.5}Sb_{1.5}Te_3$ (PDF#49-1713). No SiC diffraction peaks were detected for the samples because of the low nano-SiC amount. In addition, the 30 nm-SiC dispersed sample was chosen as a representative sample and its XRD patterns from the diffraction planes parallel and perpendicular to the SPS compression direction are shown in Fig. 1b. The two sets of peaks show excellent agreement with each other and with the standard PDF data (PDF#49-1713), illustrating the isotropy of the BM + SPS sample. Herein, the Lotgering method [40] was adopted to evaluate the orientation factor (F) of the sample as follows:

$$F = (P - P_0) / (1 - P_0), \quad (1)$$

$$P = \sum I(00l) / \sum I(hkl), \quad (2)$$

$$P_0 = \sum I_0(00l) / \sum I_0(hkl), \quad (3)$$

where P and P_0 are the ratios of the integrated intensities of all $(00l)$ planes to those of all (hkl) planes for the preferentially and randomly oriented samples, respectively. The determined F values were −0.09 and −0.03 for the 30 nm-SiC dispersed sample with the diffraction planes parallel and perpendicular to the SPS compression direction, respectively. The two negative F values demonstrate a weak $(00l)$-preferred orientation and both of these small values verify the isotropy of the sample processed by BM and SPS.

The SEM micrographs of the fracture surfaces of the samples containing SiC nanoparticles with different sizes are presented in Fig. 2. No significant differences were observed between the morphologies of the four samples. Lamellar grains with a size of several micrometers that are a typical feature of the layer-structured Bi_2Te_3-based materials can be clearly observed. Although some nanopores were observed in the four samples, the densities of all of the samples still reach >96% of the theoretical values (shown in Table 1). EDS-mapping indicates that the main Bi, Te, Sb, and Se elements are homogeneously distributed, and some Si signals were also detected (Fig. S2).

Several room-temperature properties, namely the d, σ, S, carrier concentration (p), Hall mobility (μ), and scattering parameter (r), of the samples containing SiC nanoparticles of different sizes are summarized in Table 1. The carrier concentrations show a slight reduction with increasing nano-SiC size that can be explained as follows: nano-SiC addition introduces abundant defects that dominate the increase in the carrier concentration [17], while the donor-like effect [34] generating more electrons is strengthened due to the stronger mechanical grinding effect associated with the coarser SiC nanoparticles, particularly for the raw commercial p-type $(Bi,Sb)_2Te_3$ scraps containing Se, thus reducing the hole concentration. Intriguingly, the mobility improved after nano-SiC dispersion, contributing to the increase in electrical conductivity. This phenomenon was also discussed in a previous report [31]. Generally, the structure, carrier concentration, and effective mass affect mobility. In this

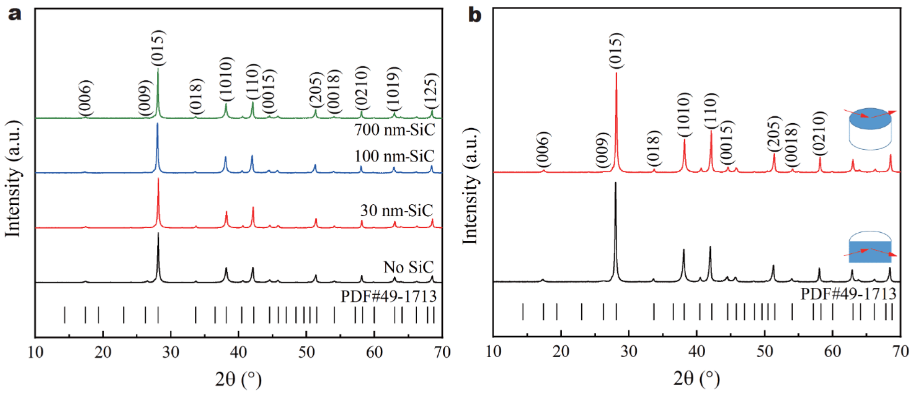

Figure 1 (a) XRD patterns of the p-type $(Bi,Sb)_2Te_3$ dispersing SiC nanoparticles with different sizes. (b) XRD patterns of the 30 nm-SiC dispersed sample with different diffraction planes as indicated in the figure.

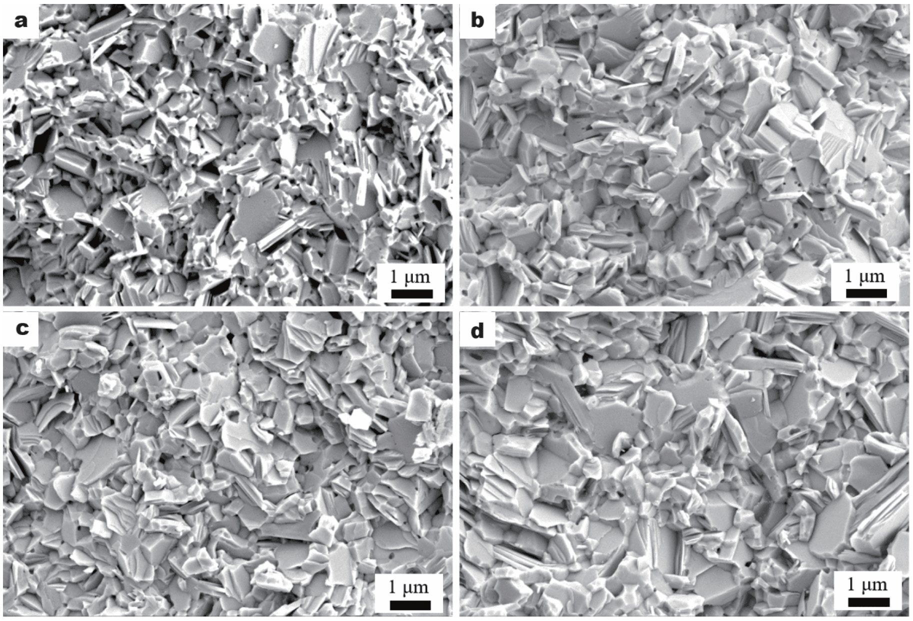

Figure 2 SEM images of the fracture surfaces of the samples. (a–d) The corresponding samples without the SiC nanoparticles, and with the dispersion of 30, 100, and 700 nm-SiC nanoparticles, respectively.

Table 1 Density (*d*), electrical conductivity (*σ*), Seebeck coefficient (*S*), carrier concentration (*p*), Hall mobility (*μ*), and scattering parameter (*r*) of the commercially available p-type $(Bi,Sb)_2Te_3$ incorporating SiC nanoparticles with different sizes at room temperature

Composition	d (g cm^{-3})	σ (S cm^{-1})	S (μV K^{-1})	p (10^{19} cm^{-3})	μ (cm^2 V^{-1} s^{-1})	r
without SiC	6.57	356.21	265.54	1.07	207.81	−0.50
30 nm-SiC	6.55	390.99	273.24	1.06	230.25	−0.40
100 nm-SiC	6.57	366.92	275.06	1.02	224.55	−0.39
700 nm-SiC	6.62	367.69	274.91	0.998	229.98	−0.41

work, the identical morphologies for the four samples have been verified by the SEM patterns. The change in the carrier concentration is insufficient to increase the mobility, as indicated by the variation in the carrier concentrations between the sample without nano-SiC and the sample containing dispersed 30 nm-SiC (Table 1). Additionally, nano-SiC dispersion does not affect the band structure and therefore does not change the effective mass. The origin of this phenomenon still needs to be explored, and here we propose several possible explanations. First, as discussed in our previous reports [17,34], nano-SiC inclusions induce the energy-filtering effect that impedes the transport of low-energy carriers while letting high-energy carriers pass smoothly, and thus may lead to the net increase of mobility. Second, the interfaces between nano-SiC and $(Bi,Sb)_2Te_3$ always have higher energies than the matrix, which may lead to the accumulation of defects [41] such as $V_{Te}^{\bullet\bullet}$, $V_{Se}^{\bullet\bullet}$, and Bi'_{Te} at the interfaces, thus reducing the random distribution of the carrier scattering centers and increasing the mobility. Third, the intrinsic high mobility and conductivity of SiC [42,43] may also promote carrier transport, and therefore directly increase the mobility. It is presumed that the SiC nanoparticles with finer sizes may also lead to an increase in mobility, contributing to the further rise of the electrical conductivity.

Fig. 3 shows the electrical properties of the samples that contain SiC nanoparticles of different sizes. Fig. 3a shows the measured high-temperature carrier concentration. All of the samples exhibit evidently increased carrier concentration with increasing temperature due to the significant intrinsic excitation associated with the lower carrier concentration at room temperature. In contrast to the temperature dependence of mobility (inset of Fig. 3a), all of the nano-SiC dispersed samples show lower carrier concentration compared with the sample without nano-

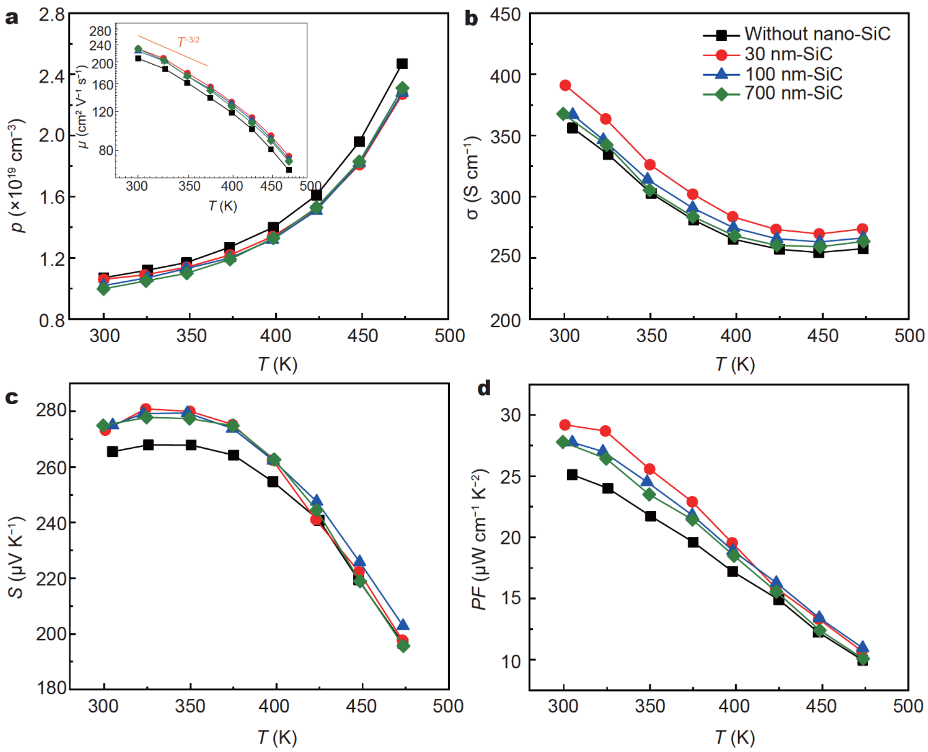

Figure 3 Electrical properties of the commercially available p-type (Bi,Sb)$_2$Te$_3$ containing dispersed SiC nanoparticles of different sizes. (a) Carrier concentration (the inset shows the mobility), (b) electrical conductivity, (c) Seebeck coefficient, and (d) power factor.

SiC in the entire temperature range. The high-temperature mobility appears to be related to the temperature according to $\mu \propto T^{-3/2}$, indicating the key role of acoustic-phonon-dominated scattering for all of the samples. For electrical conductivity (Fig. 3b), all of the samples exhibit similar variation trends: the conductivity first decreased until 450 K and then increased slightly, indicating degenerate semiconductor behavior. The increase at high temperatures is attributed to the intrinsic excitation. The electrical conductivity of the 30 nm-SiC dispersed sample displays significant improvement compared with those of the other samples over the entire temperature range due to the increased mobility, as indicated by the data presented in Table 1 and the inset of Fig. 3a.

Fig. 3c shows the Seebeck coefficients. All of the samples exhibit the same trends. The reduction at high temperature is also attributed to the increased intrinsic excitations. All of the nano-SiC dispersed samples exhibit improved Seebeck coefficients compared with the sample without nano-SiC, which is not related to the carrier concentration variation, as indicated by the Pisarenko plot shown in Fig. S3. Here, the scattering parameter r is calculated and the results are presented in Table 1. A detailed description of the calculation procedure can be found in the Supplementary information. All of the nano-SiC dispersed samples show enhanced r compared with the sample without nano-SiC, supporting the variation in Fig. S3. The enhancement of r covers two contributions: the energy-filtering effect and the composition (average) effect. For 3C-SiC, the lattice constant (a = 0.436 nm) is similar to those of p-type (Bi,Sb)$_2$Te$_3$ (a = 0.429 nm and c = 3.052 nm), and this may give rise to coherent interfaces between 3C-SiC and p-type (Bi,Sb)$_2$Te$_3$. The presence of such interfaces significantly enhances the energy-filtering effectand increases the Seebeck coefficient [17,34]. The composition (average) effect is due to the 4H- and 6H-SiC phases. According to the XRD results obtained for nano-SiC (shown in Fig. S1), the contents of 4H- and 6H-SiC are estimated as 3.7% of 4H-SiC in 30 nm-SiC, 4.3% of 4H-SiC in 100 nm-SiC, and 3.3% of 6H-SiC in 700 nm -SiC. These types of SiC may also contribute to the enhancement of the Seebeck coefficient because of their wide band gaps and large Seebeck coefficients [17] despite the mismatch of their lattice constants with those of p-type (Bi,Sb)$_2$Te$_3$ (shown in Table S1). The Seebeck coefficients of the 100 nm-SiC dispersed sample are the highest above 400 K. SiC is stable, so we speculate that the different sized SiC nanoparticles may cause different temperature-dependent energy distributions. At higher temperatures, 100 nm-SiC nanoparticles may more effectively scatter the low-energy carriers and lead to higher Seebeck coefficient. To summarize, the dispersion of SiC nanoparticles significantly improves the Seebeck coefficient of p-type $(Bi,Sb)_2Te_3$ regardless of the SiC nanoparticle size. The highest power factor (PF) of ~29 $\mu W\ cm^{-1}\ K^{-2}$ was achieved in the 30 nm-SiC dispersed sample (shown in Fig. 3d). Besides, the electronic quality factors (B_E) [44] which can be used for determining the maximum of PF were also calculated (shown in Fig. S4). It is clear that the B_E increased after SiC nanoparticles dispersion, indicating an enhancement in electronic properties.

Fig. 4a shows the thermal conductivities of the commercially available p-type $(Bi,Sb)_2Te_3$ with dispersed SiC nanoparticles of different sizes. For all of the samples, the thermal conductivity increases monotonically with increasing temperature, which is attributed to the intrinsic excitation. The thermal conductivity of the 700 nm-SiC dispersed sample is higher than those of the other samples. The lattice (κ_{lat}) plus bipolar (κ_b) thermal conductivity contributions show clearly that the 700 nm-SiC dispersed sample possesses the highest ($\kappa_{lat} + \kappa_b$) values over the entire temperature range. Since the three types of SiC (3C, 4H and 6H) have the same intrinsic high thermal conductivity (Table S1), the differences among the thermal conductivities of the samples should be more attributed to the difference in the sizes of the SiC nanoparticles rather than to the different SiC types. The coarser SiC nanoparticle has lower specific surface area, resulting in weak phonon scattering and a prominent composition (average) effect. However, when the size of the nano-SiC decreases to 100 nm or much lower, the scattering effect of the nanoparticles on the phonons gradually becomes pronounced, leading to little change of the ($\kappa_{lat} + \kappa_b$) value compared with the sample without nano-SiC. Here, we adopted a widely accepted model to estimate the phonon mean free path l_{ph} [45,46]:

$$\kappa_{lat} = \frac{1}{3} C_V\, v l_{ph}, \tag{4}$$

where C_V and v are the specific heat at constant volume and the average sound velocity. The calculated results are plotted in the inset of Fig. 4a and show that the phonon mean free path decreases with decreasing SiC nanoparticle size. It can be inferred that the SiC nanoparticles with the sizes of 10, 5 nm or much finer may lead to a stronger phonon scattering effect, and the lattice thermal conductivity may be further reduced.

The ZT values presented in Fig. 4b display a clear trend. The 30 nm-SiC dispersed sample benefiting from the excellent electrical transport properties and the nearly unchanged lattice thermal conductivity possesses the highest ZT value of 1.12 at 325 K. Although these results confirm the effect of SiC dispersion, the obtained maximum ZT of 1.12 is not an outstanding value compared with the previously reported ZT values [17]. This is most likely due to the compositional differences. In this work, the commercial scraps were used for the purpose of material recycling, so that the sample without SiC also showed lower ZT values because its composition was optimized for zone-melting processing rather than for powder processing [47]. Nevertheless, these results are still an instructive demonstration that $(Bi,Sb)_2Te_3$ nanocomposites with high TE performance can be obtained by selecting nanoparticles with an appropriate size.

Microstructure analysis was performed for the 30 nm

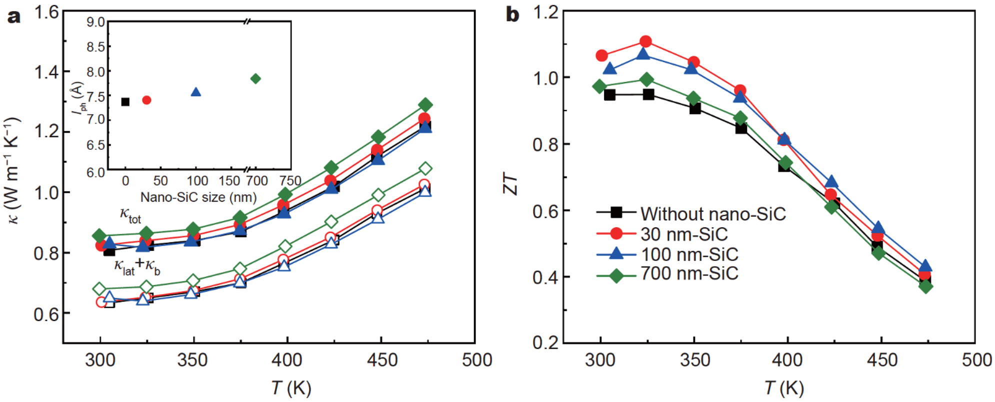

Figure 4 (a) Thermal conductivity with the inset showing the calculated phonon mean free path l_{ph}. (b) ZT values of the commercially available p-type $(Bi,Sb)_2Te_3$ containing dispersed SiC nanoparticles of different sizes.

-SiC dispersed sample because of its relatively high *ZT* value. Fig. 5a presents the low-magnification TEM image together with the EDS results showing the SiC nanoparticles distributed in the $(Bi,Sb)_2Te_3$ matrix. Fig. 5b and Fig. S5 exhibit some Moiré patterns and twinning characteristics (as observed in the region indicated by the red ellipse in Fig. 5b), that appear to be common in the BiSbTe system [35,38,48] due to the twist of the adjacent grains and the low stacking fault energy [48,49], respectively. The selected area electron diffraction (SAED) pattern (inset of Fig. 5b) displays two sets of diffraction spots, corresponding to twinning diffraction. The high-resolution TEM (HRTEM) image (Fig. 5c) from the region marked by the red ellipse in Fig. 5b further verifies the twinning structure. Fig. 5d and inset show the inverse fast Fourier transform (IFFT) images corresponding to regions C1 and C2 in Fig. 5c, respectively, that exhibit a small number of curved lattice fringes and dislocations. These defects, including nanoparticles, twinning structures and dislocations, do in fact exert a strong influence on phonon transport. However, the $(\kappa_{\mathrm{lat}} + \kappa_{\mathrm{b}})$ value shows little change compared with that of the sample without nano-SiC, which should be attributed to the small amount of the defects and the high intrinsic thermal conductivity of SiC. It was observed that the p-type $(Bi,Sb)_2Te_3$ and 4H-SiC are connected *via* a transition region possibly due to the mismatch between their lattice constants (shown in Table S1), as presented in Fig. 5e. However, clear interfaces are formed between p-type $(Bi,Sb)_2Te_3$ and 3C-SiC (Fig. 5f) due to their similar lattice

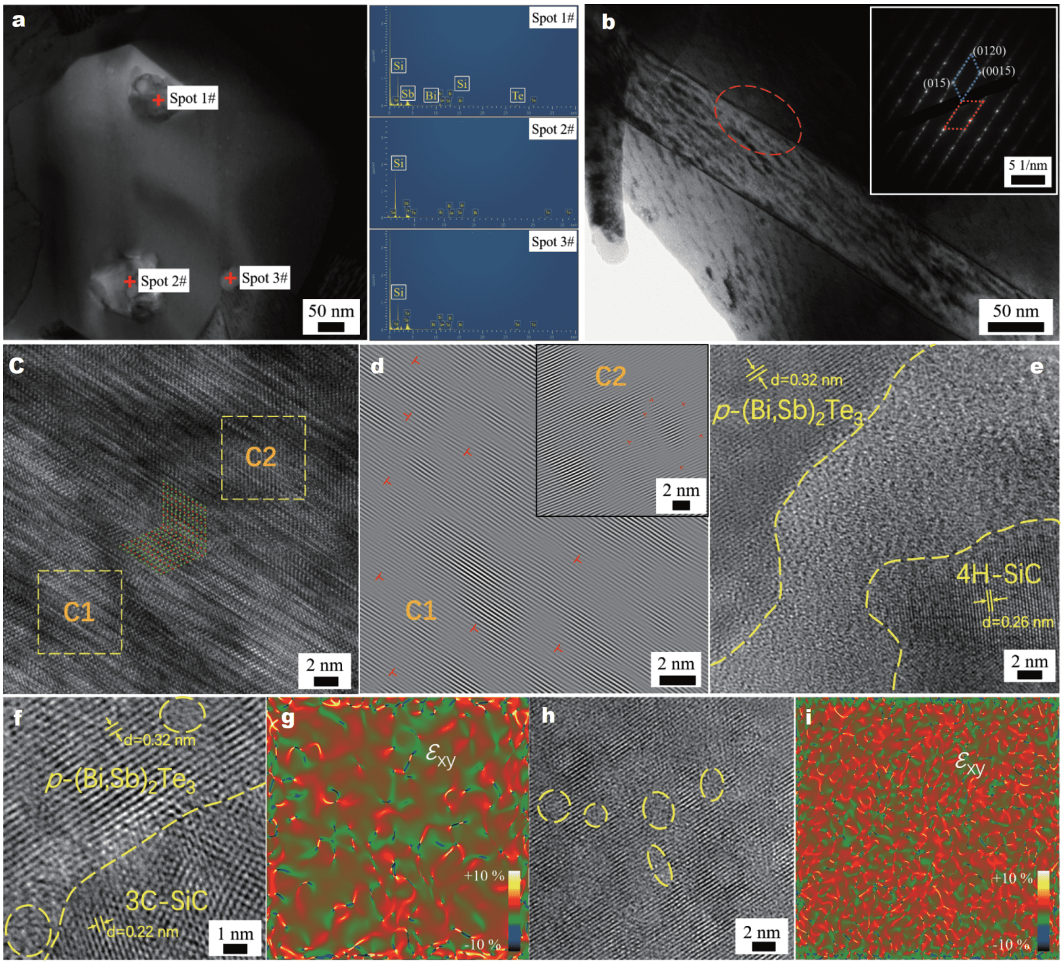

Figure 5 Microstructure of the commercially available p-type $(Bi,Sb)_2Te_3$ containing dispersed 30 nm-SiC. (a) Low-magnification TEM image and EDS results. (b) TEM image with the corresponding SAED diffraction spots shows a typical twinning characteristic. (c) HRTEM image from the region indicated by the red ellipse in (b). (d) IFFT images from regions C1 and C2 (inset) in (c). HRTEM images of (e, f) the 4H-SiC/p-type $(Bi,Sb)_2Te_3$ and 3C-SiC/p-type $(Bi,Sb)_2Te_3$ interfaces, respectively; (h) the p-type $(Bi,Sb)_2Te_3$ matrix away from nano-SiC. (g, i) The geometric phase analysis (GPA) images corresponding to (f) and (h), respectively. Some dislocation regions are observed as indicated by the yellow circles in (f) and (h).

constants which is the prerequisite for generating the energy-filtering effect [50,51]. Some dislocation regions can also be observed in the p-type $(Bi,Sb)_2Te_3$ matrix near and away from SiC, as indicated by the yellow circles in Fig. 5f, h, respectively. Fig. 5g, i exhibit the corresponding geometric phase analysis (GPA) images of Fig. 5f, h, respectively, and mass tensile strain regions are observed in both. These strain regions were attributed to the intense BM process and were not completely eliminated upon sintering for only 5 min. This is also a reason for the measured lower lattice thermal conductivity compared with that of the commercial ingot (Fig. S6).

κ_{lat} is a crucial parameter in TE research focusing on ZT optimization because it can be regulated relatively independently of the electronic-structure-dependent parameters S and σ. For the materials investigated in this work, κ_{lat} is intertwined with κ_b, making its further investigation difficult. However, in fact, phonon-phonon Umklapp scattering dominates heat transport when the temperature is well above the Debye temperature of Bi_2Te_3 materials (162 K), and therefore the κ_{lat} and κ_b contributions can be separated by using the $\kappa_{lat} \propto T^{-1}$ [52,53] relation in these conditions. κ_{lat} can be approximated by $(\kappa - \kappa_e)$ if intrinsic excitation can be neglected. Therefore, κ_{lat} at high temperatures can be obtained by fitting the $(\kappa - \kappa_e)$ values to $\kappa_{lat} = aT^{-1} + b$ [52,54] (where a and b are fitting parameters) in an appropriate temperature range. Here, we chose 200–250 K as the temperature range of the fitting for the 30 nm-SiC dispersed sample. The separated κ_{lat} and κ_b along with the fitted curve are shown in Fig. 6a. It is observed that κ_{lat} shows a small range of decreased values from 300 to 475 K compared with previous studies [52,55]; this is due to the lower nanoparticle number density and dislocation density (as indicated by the (HR)TEM images presented in Fig. 5) that weaken the mid-high frequency phonon scattering. Here, the Debye-Callaway model (Table S2) was adopted to evaluate the effect of the SiC nanoparticles with different sizes on κ_{lat}, with the results shown in Fig. 6b. The calculation method is the same as that in our previous report [34]. The related parameters are listed in the Supplementary information. The calculated κ_{lat} values are lower than the corresponding experimental values due to the lack of consideration of the SiC thermal conductivity in the calculation. It is found that the calculated κ_{lat} decreases gradually until the nano-SiC size decreases to 10 nm, and then reduces sharply when the nano-SiC size continues to decrease to 1 nm, supporting our above-mentioned inference. The size of the finer SiC nanoparticles is closer to the phonon mean free path of p-type $(Bi,Sb)_2Te_3$, producing more intense phonon scattering and thereby decreasing κ_{lat}.

SiC nanocomposite combined with compositional and processing modifications

Introduction and extrusion of excess Te element in Bi_2Te_3-based compounds has been proved to be an effective method for TE performance enhancement [35–37]. Herein, excess Te was introduced into the commercially available p-type $(Bi,Sb)_2Te_3$ scraps on the basis of dispersion with 0.4 vol% 30 nm-SiC. To expel Te more effectively, the SPS conditions were modified to 743 K and 15 min under 50 MPa. Fig. S7 shows the TE properties. All of the samples with expelled excess Te show normal variation compared with the sample without expelled excess Te, namely the electrical conductivity

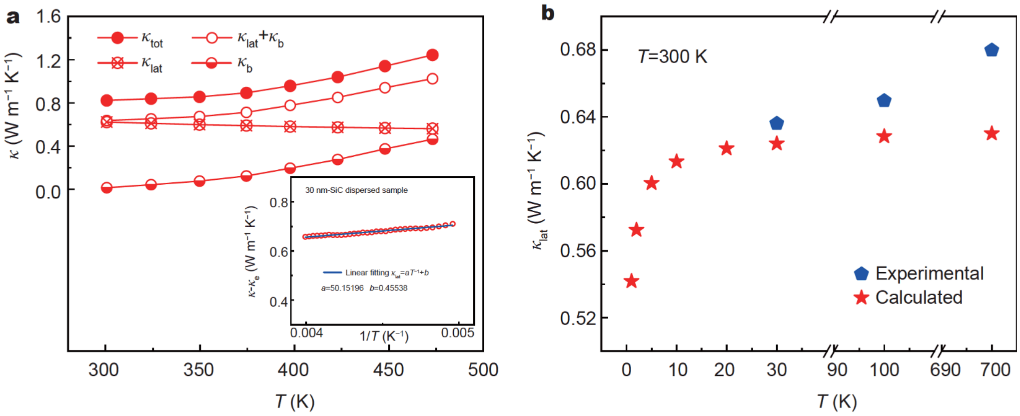

Figure 6 (a) Separated κ_{lat} together with κ_{tot} and κ_b of the 30 nm-SiC dispersed sample. The inset shows the fitted linear relationship. (b) Nano-SiC size-dependent κ_{lat} in p-type $(Bi,Sb)_2Te_3$-based composite calculated *via* the Debye-Callaway model at room temperature. The corresponding experimental values are also included.

is enhanced and the Seebeck coefficient is reduced, which should be attributed to the increased carrier concentration and mobility resulting from the expulsion of excess Te (Fig. 7f). It appears that the sample still manifests the enhancement effect of the Seebeck coefficient even though it suffers from the expulsion of excess Te (as shown in Fig. S7c) that can be ascribed to the nano-SiC dispersion, as analyzed above. Naturally, the thermal conductivity increases with the expulsion of excess Te due to the increased electrical conductivities. The highest *ZT* value of 1.15 was obtained in 0.4 vol% 30 nm-SiC dispersed p-type $(Bi,Sb)_2Te_3$ with the expulsion of 2 wt% excess Te.

Our previous work proved that optimization of the matrix composition is crucial for obtaining improved TE performance of Bi_2Te_3-based compounds and showed that the modulated composition with the Bi/Sb ratio of 0.4/1.6 is more appropriate for the samples processed using the BM method [34]. Hence, based on the optimized nano-SiC composite (0.4 vol% 30 nm-SiC) and the expulsion of excess Te (2 wt%), the matrix composition was modulated to achieve the Bi/Sb ratio of 0.4/1.6. The TE properties of the resultant sample are shown in Fig. 7. The electrical conductivity of the sample with Bi/Sb ratio of 0.4/1.6 is greatly improved compared with the composition-unmodulated samples, while the Seebeck coefficient drops markedly. Both variations are due to the significantly increased carrier concentration (Fig. 7f). Compared with the original matrix composition of commercial $(Bi,Sb)_2Te_3$ with the Bi/Sb ratio of approximately 0.5/1.5, the modulated composition has a greater Sb content, contributing more antisite defects Sb'_{Te} and hole carriers. Moreover, the excess Te compensates the Te vacancies and inhibits the donor-like effect to some extent, thereby suppressing the generation of electrons [34]. The extrusion of excess Te during the SPS process may also lead to the grain rearrangement [35]. The improved SPS temperature and duration time (743 K/15 min) also promote the grain growth. Therefore, the mobility is unaffected by the increased hole concentration and improves only slightly. The PF attains the maximum value of 39 $\mu W\ cm^{-1}\ K^{-2}$ due to the synergistic modulation. Meanwhile, the thermal conductivity of the matrix-composition-modified sample (Bi/Sb = 0.4/1.6) increases compared with the composition-unmodulated samples; this is due to the substantial contribution of the hole carriers. In addition, the thermal conductivity is noticeably lower than those of other samples after 400 K, which is ascribed to the suppressed bipolar thermal conductivity related to the higher carrier concentration. Eventually, the

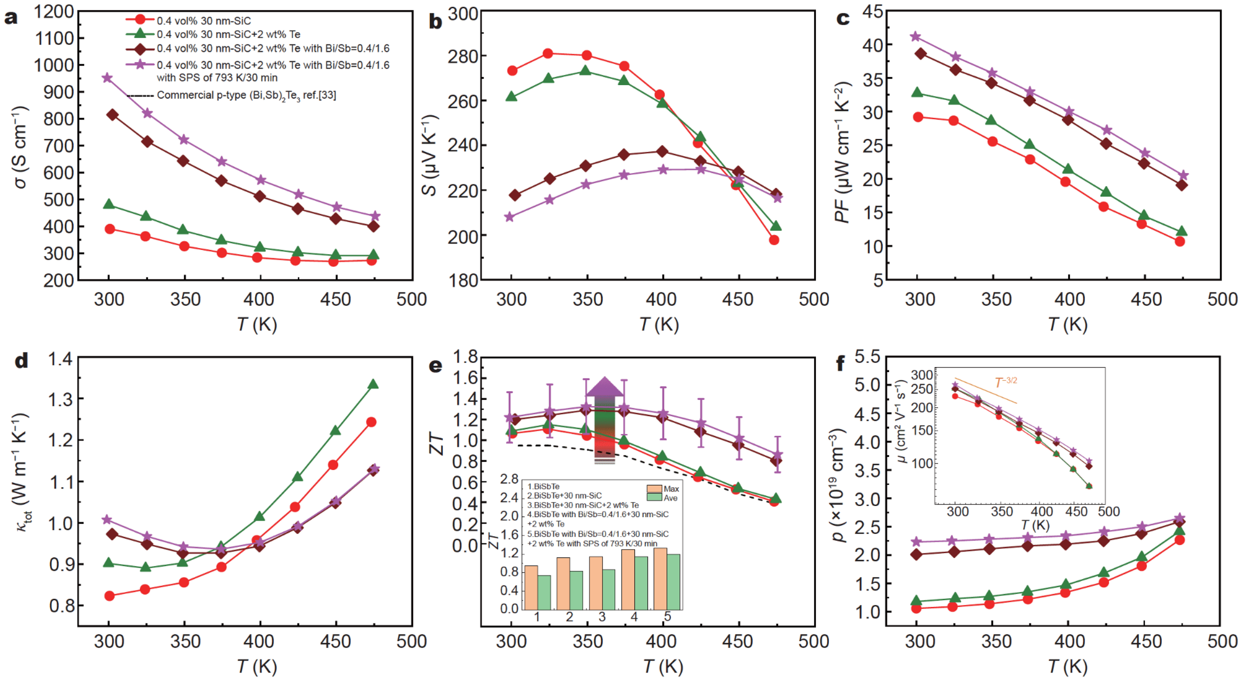

Figure 7 Temperature-dependent TE properties of the commercially available p-type $(Bi,Sb)_2Te_3$ with different TE performance modulation strategies. (a) Electrical conductivity; (b) Seebeck coefficient; (c) power factor; (d) thermal conductivity; (e) *ZT* value (the error bars are ± 20%) and the maximum and average *ZT* shown in the inset (derived from 300 to 475 K); (f) carrier concentration (the inset shows the mobility).

highest *ZT* value of 1.30 is achieved as shown in Fig. 7e.

To benefit from the advantages of improved SPS temperature and prolonged SPS duration time, as well as the optimized matrix composition, the SPS conditions of the matrix-composition-optimized sample was further modified to 793 K and 30 min, and the TE performance of the obtained sample is shown in Fig. 7. The improved SPS temperature and prolonged duration time may further modulate the defects and lead to more grown grains, which are favorable for obtaining higher carrier concentration and mobility (shown in Fig. 7f), respectively. Therefore, the electrical conductivity improved to 951 S cm^{-1} at room temperature compared with that of the sample possessing the same composition but SPS-processed at 743 K/15 min. Although the Seebeck coefficient decreased, a PF as high as 41 μW cm^{-1} K^{-2} was achieved. The increase in thermal conductivity is ascribed to the improved carrier concentration. The peak *ZT* value of 1.33 was obtained, and the overall *ZT* was also substantially improved as shown in Fig. 7e.

The inset of Fig. 7e shows the maximum and average *ZT* (ZT_{max} and ZT_{ave}) values (derived from the temperature range of 300–475 K) of the commercial p-type $(Bi,Sb)_2Te_3$ scraps obtained following different TE performance enhancement strategies. Compared with the raw $(Bi,Sb)_2Te_3$ materials, the maximum and average ZT increased by 40% and 62% due to the synergistic optimization of SiC nanoparticles dispersion, extrusion of excess Te, matrix composition modulation, and SPS conditions' optimization. Thus, the combination of multiple strategies is demonstrated to be beneficial for the enhancement of the TE performance of the p-type $(Bi,Sb)_2Te_3$ materials.

CONCLUSIONS

Nano-SiC/$(Bi,Sb)_2Te_3$ composites were synthesized using commercially available p-type $(Bi,Sb)_2Te_3$ scraps and SiC nanoparticles of different sizes. The dispersion of nano-SiC results in increased electrical conductivity and Seebeck coefficient, decoupling both the properties to a certain extent. This effect becomes more pronounced with the decreasing size of the SiC nanoparticles. The enhancement in the Seebeck coefficient appears to be independent of the size or crystal phases of the SiC nanoparticles. The influence of the SiC nanoparticles on thermal conductivity is related to the competition between the composition effects and scattering effects, i.e., the nanoparticles with the sizes of 100 nm or much less have a more pronounced effect to increase phonon scattering, while larger SiC nanoparticles present a greater composition (average) effect. The Debye-Callaway model calculations indicate that a more prominent phonon scattering effect is obtained with increasing reduction of the nano-SiC size. Eventually, the highest *ZT* value of 1.12 was obtained in the 30 nm-SiC dispersed sample. Furthermore, excess Te was introduced and expelled based on the 30 nm-SiC dispersed sample, and together with the optimization of matrix composition modulation and SPS conditions enabled the achievement of the peak *ZT* value of 1.33. This work paves the way for recycling commercial Bi_2Te_3 scraps, and provides guidance for selecting nanoparticles with an appropriate size (smaller nanoparticles are better for enhancing the TE performance of Bi_2Te_3 materials); finally, our work highlights the importance of synergistic optimization with multiple strategies. This guiding principle can also be expected to be widely applicable to other promising TE materials.

Received 20 January 2021; accepted 15 February 2021;

1 He R, Schierning G, Nielsch K. Thermoelectric devices: A review of devices, architectures, and contact optimization. Adv Mater Technol, 2018, 3: 1700256

2 Kishore RA, Nozariasbmarz A, Poudel B, *et al.* Ultra-high performance wearable thermoelectric coolers with less materials. Nat Commun, 2019, 10: 1765

3 Yang L, Chen ZG, Dargusch MS, *et al.* High performance thermoelectric materials: Progress and their applications. Adv Energy Mater, 2018, 8: 1701797

4 Liu W, Bai S. Thermoelectric interface materials: A perspective to the challenge of thermoelectric power generation module. J Materiomics, 2019, 5: 321–336

5 Zhu T, Liu Y, Fu C, *et al.* Compromise and synergy in high-efficiency thermoelectric materials. Adv Mater, 2017, 29: 1605884

6 Li S, Li X, Ren Z, *et al.* Recent progress towards high performance of tin chalcogenide thermoelectric materials. J Mater Chem A, 2018, 6: 2432–2448

7 Cai B, Hu H, Zhuang HL, *et al.* Promising materials for thermoelectric applications. J Alloys Compd, 2019, 806: 471–486

8 Biswas K, He J, Zhang Q, *et al.* Strained endotaxial nanostructures with high thermoelectric figure of merit. Nat Chem, 2011, 3: 160–166

9 He J, Androulakis J, Kanatzidis MG, *et al.* Seeing is believing: Weak phonon scattering from nanostructures in alkali metal-doped lead telluride. Nano Lett, 2012, 12: 343–347

10 Poudel B, Hao Q, Ma Y, *et al.* High-thermoelectric performance of nanostructured bismuth antimony telluride bulk alloys. Science, 2008, 320: 634–638

11 Hong M, Chen ZG, Yang L, *et al.* Achieving *zT* > 2 in p-type $AgSbTe_{2-x}Se_x$ alloys *via* exploring the extra light valence band and introducing dense stacking faults. Adv Energy Mater, 2018, 8: 1702333

12 Fu C, Zhu T, Pei Y, *et al.* High band degeneracy contributes to high thermoelectric performance in p-type half-Heusler compounds. Adv Energy Mater, 2014, 4: 1400600

13 Pei Y, Wang H, Snyder GJ. Band engineering of thermoelectric

materials. Adv Mater, 2012, 24: 6125–6135

14 Gayner C, Amouyal Y. Energy filtering of charge carriers: Current trends, challenges, and prospects for thermoelectric materials. Adv Funct Mater, 2020, 30: 1901789

15 Faleev SV, Léonard F. Theory of enhancement of thermoelectric properties of materials with nanoinclusions. Phys Rev B, 2008, 77: 214304

16 Paul B, Kumar V A, Banerji P. Embedded Ag-rich nanodots in PbTe: Enhancement of thermoelectric properties through energy filtering of the carriers. J Appl Phys, 2010, 108: 064322

17 Li J, Tan Q, Li JF, *et al.* BiSbTe-based nanocomposites with high *ZT*: The effect of SiC nanodispersion on thermoelectric properties. Adv Funct Mater, 2013, 23: 4317–4323

18 Hwang JY, Kim J, Kim HS, *et al.* Effect of dislocation arrays at grain boundaries on electronic transport properties of bismuth antimony telluride: Unified strategy for high thermoelectric performance. Adv Energy Mater, 2018, 8: 1800065

19 Meng X, Liu Z, Cui B, *et al.* Grain boundary engineering for achieving high thermoelectric performance in n-type skutterudites. Adv Energy Mater, 2017, 7: 1602582

20 Zhou C, Chung I. Nanoscale defect structures advancing high performance n-type PbSe thermoelectrics. Coord Chem Rev, 2020, 421: 213437

21 Qiu J, Yan Y, Xie H, *et al.* Achieving superior performance in thermoelectric $Bi_{0.4}Sb_{1.6}Te_{3.72}$ by enhancing texture and inducing high-density line defects. Sci China Mater, 2021, 64: 1507–1520

22 Xiao Y, Zhao LD. Seeking new, highly effective thermoelectrics. Science, 2020, 367: 1196–1197

23 Cai B, Li J, Sun H, *et al.* Sodium doped polycrystalline SnSe: High pressure synthesis and thermoelectric properties. J Alloys Compd, 2017, 727: 1014–1019

24 Zhou Y, Zhao LD. Promising thermoelectric bulk materials with 2D structures. Adv Mater, 2017, 29: 1702676

25 Liu Y, Ding J, Xu B, *et al.* Enhanced thermoelectric performance of La-doped BiCuSeO by tuning band structure. Appl Phys Lett, 2015, 106: 233903

26 Wang D, Huang Z, Zhang Y, *et al.* Extremely low thermal conductivity from bismuth selenohalides with 1D soft crystal structure. Sci China Mater, 2020, 63: 1759–1768

27 Pei J, Cai B, Zhuang HL, *et al.* Bi_2Te_3-based applied thermoelectric materials: Research advances and new challenges. Natl Sci Rev, 2020, 7: 1856–1858

28 Madavali B, Kim HS, Lee KH, *et al.* Enhanced Seebeck coefficient by energy filtering in Bi-Sb-Te based composites with dispersed Y_2O_3 nanoparticles. Intermetallics, 2017, 82: 68–75

29 Kim KT, Min TS, Kim SD, *et al.* Strain-mediated point defects in thermoelectric p-type bismuth telluride polycrystalline. Nano Energy, 2019, 55: 486–493

30 Li C, Ma S, Wei P, *et al.* Magnetism-induced huge enhancement of the room-temperature thermoelectric and cooling performance of p-type BiSbTe alloys. Energy Environ Sci, 2020, 13: 535–544

31 Zhang D, Lei J, Guan W, *et al.* Enhanced thermoelectric performance of BiSbTe alloy: Energy filtering effect of nanoprecipitates and the effect of SiC nanoparticles. J Alloys Compd, 2019, 784: 1276–1283

32 Hu L, Meng F, Zhou Y, *et al.* Leveraging deep levels in narrow bandgap $Bi_{0.5}Sb_{1.5}Te_3$ for record-high zT_{ave} near room temperature. Adv Funct Mater, 2020, 30: 2005202

33 Liu DW, Li JF, Chen C, *et al.* Effects of SiC nanodispersion on the thermoelectric properties of p-type and n-type Bi_2Te_3-based alloys. J Elec Materi, 2010, 40: 992–998

34 Cai B, Zhuang HL, Cao Q, *et al.* Practical high-performance $(Bi,Sb)_2Te_3$-based thermoelectric nanocomposites fabricated by nanoparticle mixing and scrap recycling. ACS Appl Mater Interfaces, 2020, 12: 16426–16435

35 Deng R, Su X, Zheng Z, *et al.* Thermal conductivity in $Bi_{0.5}Sb_{1.5}Te_{3+x}$ and the role of dense dislocation arrays at grain boundaries. Sci Adv, 2018, 4: eaar5606

36 Kim SI, Lee KH, Mun HA, *et al.* Dense dislocation arrays embedded in grain boundaries for high-performance bulk thermoelectrics. Science, 2015, 348: 109–114

37 Pan Y, Qiu Y, Witting I, *et al.* Synergistic modulation of mobility and thermal conductivity in $(Bi,Sb)_2Te_3$ towards high thermoelectric performance. Energy Environ Sci, 2019, 12: 624–630

38 Zhuang HL, Pan Y, Sun FH, *et al.* Thermoelectric Cu-doped $(Bi,Sb)_2Te_3$: Performance enhancement and stability against high electric current pulse. Nano Energy, 2019, 60: 857–865

39 Du B, Lai X, Liu Q, *et al.* Spark plasma sintered bulk nanocomposites of $Bi_2Te_{2.7}Se_{0.3}$ nanoplates incorporated Ni nanoparticles with enhanced thermoelectric performance. ACS Appl Mater interfaces, 2019, 11: 31816–31823

40 Lotgering FK. Topotactical reactions with ferrimagnetic oxides having hexagonal crystal structures—I. J Inorg Nucl Chem, 1959, 9: 113–123

41 Wu CF, Wang H, Yan Q, *et al.* Doping of thermoelectric PbSe with chemically inert secondary phase nanoparticles. J Mater Chem C, 2017, 5: 10881–10887

42 Mnatsakanov TT, Levinshtein ME, Pomortseva LI, *et al.* Carrier mobility model for simulation of SiC-based electronic devices. Semicond Sci Technol, 2002, 17: 974–977

43 Lankau V, Martin HP, Hempel-Weber R, *et al.* Preparation and thermoelectric characterization of SiC-B_4C composites. J Elec Materi, 2010, 39: 1809–1813

44 Zhang X, Bu Z, Shi X, *et al.* Electronic quality factor for thermoelectrics. Sci Adv, 2020, 6: eabc0726

45 Zheng Y, Zhang Q, Su X, *et al.* Mechanically robust BiSbTe alloys with superior thermoelectric performance: A case study of stable hierarchical nanostructured thermoelectric materials. Adv Energy Mater, 2015, 5: 1401391

46 Dugdale JS, MacDonald DKC. Lattice thermal conductivity. Phys Rev, 1955, 98: 1751–1752

47 Pan Y, Wei TR, Wu CF, *et al.* Electrical and thermal transport properties of spark plasma sintered n-type $Bi_2Te_{3-x}Se_x$ alloys: The combined effect of point defect and Se content. J Mater Chem C, 2015, 3: 10583–10589

48 Yu Y, He DS, Zhang S, *et al.* Simultaneous optimization of electrical and thermal transport properties of $Bi_{0.5}Sb_{1.5}Te_3$ thermoelectric alloy by twin boundary engineering. Nano Energy, 2017, 37: 203–213

49 Cao YQ, Zhao XB, Zhu TJ, *et al.* Syntheses and thermoelectric properties of Bi_2Te_3/Sb_2Te_3 bulk nanocomposites with laminated nanostructure. Appl Phys Lett, 2008, 92: 143106

50 Jo S, Park SH, Ban HW, *et al.* Simultaneous improvement in electrical and thermal properties of interface-engineered BiSbTe nanostructured thermoelectric materials. J Alloys Compd, 2016, 689: 899–907

51 Yang J, Xi L, Qiu W, *et al.* On the tuning of electrical and thermal transport in thermoelectrics: An integrated theory-experiment perspective. npj Comput Mater, 2016, 2: 15015

52 Hao F, Xing T, Qiu P, *et al.* Enhanced thermoelectric performance

in n-Type Bi$_2$Te$_3$-based alloys *via* suppressing intrinsic excitation. ACS Appl Mater Interfaces, 2018, 10: 21372–21380

53 Morelli DT, Jovovic V, Heremans JP. Intrinsically minimal thermal conductivity in cubic I-V-VI2 semiconductors. Phys Rev Lett, 2008, 101: 035901

54 Hao F, Qiu P, Tang Y, *et al.* High efficiency Bi$_2$Te$_3$-based materials and devices for thermoelectric power generation between 100 and 300°C. Energy Environ Sci, 2016, 9: 3120–3127

55 Xing T, Liu R, Hao F, *et al.* Suppressed intrinsic excitation and enhanced thermoelectric performance in Ag$_x$Bi$_{0.5}$Sb$_{1.5-x}$Te$_3$. J Mater Chem C, 2017, 5: 12619–12628

Acknowledgements This work was supported by the Basic Science Center Project of the National Natural Science Foundation of China (51788104), and the National Key R&D Program of China (2018YFB0703603).

Author contributions Cai B and Li JF designed the project; Cai B, Pei J, Dong J, Zhuang HL, Gu J, Hu H and Lin Z conducted the experiments and analyzed the data; Cao Q supplied the raw materials; Cai B and Li JF wrote the paper. All authors contributed to the general discussion.

Conflict of interest The authors declare that they have no conflict of interest.

Supplementary information Experimental details and supporting data are available in the online version of the paper.

Bowen Cai is now a post-doctor working at the School of Materials Science and Engineering, Tsinghua University. His current research interests include thermoelectric materials and high-pressure technology. He holds a BE degree from Xi'an University of Technology and a PhD degree from Yanshan University in Qinhuangdao, China.

Jing-Feng Li is a professor at Tsinghua University, China. He graduated from Huazhong University of Science and Technology (China) in 1984, and obtained his doctor degree from Tohoku University (Japan) in 1991. After working at Tohoku University as an assistant professor from 1992 to 1997 and an associate professor from 1997 to 2002, he joined Tsinghua University as a full professor in 2002. His research interests include piezoelectric ceramics, composites and films for applications in microelectromechanical systems, thermoelectric materials and devices, materials microfabrication, ceramic processing and mechanical properties.

(Bi,Sb)$_2$Te$_3$/SiC纳米复合材料的热电性能增强：纳米SiC的尺寸和组分调控的影响

蔡博文[1]，裴俊[1]，董金峰[1]，庄华鹭[1]，顾津宇[1]，曹茜[2]，胡海华[1]，林子皓[1]，李敬锋[1*]

摘要 纳米复合是增强材料热电性能的有效手段，特别是纳米SiC粉末常被用来制备基于Bi$_2$Te$_3$的纳米复合材料，但是纳米粒子的尺寸对热电性能的影响并不清楚. 本文中，我们制备了一系列不同粒度的纳米SiC弥散于BiSbTe基体的复合材料，并系统研究了其热电性能，发现纳米粒子的尺寸对BiSbTe材料电学性能有显著影响. 小尺寸的纳米SiC复合会产生更高的电导率，纳米SiC的复合会增强材料的Seebeck系数，但这一增强与SiC的尺寸并无显著关联; 另外，小尺寸的纳米SiC能够在一定程度上散射声子，而较大尺寸的纳米SiC却会使热导率增加，当纳米SiC尺寸为30 nm时，复合材料的*ZT*值达到了1.12，相比基体材料(*ZT*值为0.95)提高了18%. 之后，通过优化基体组分、液相助烧以及优化烧结条件，材料的*ZT*值进一步提升到了1.33. 本文证明，在BiSbTe材料中弥散分布小尺寸的纳米SiC能更有效地增强热电性能. 此外，组分调控以及处理工艺的优化对于高性能的(Bi,Sb)$_2$Te$_3$/SiC纳米复合材料的获得必不可少.